# Study of GTA-Welded Joints of ZW61 Magnesium Alloy — Effect of Welding Current on the Microstructure and Mechanical Properties

## The welded joints' microstructure evolution and softening mechanism as well as the effect of limiting heat input were concretely analyzed

BY W. ZHOU, Q. LE, Q. LIAO, Y. SHI, T. WANG, AND W. HU


## Abstract

An attempt has been made to weld ZW61 magnesium alloy extruded plates by gas tungsten arc welding (GTAW). In this paper, the zone with the largest average grain size in the welded joint was the fusion zone (FZ) rather than the heat-affected zone (HAZ). The grains of the FZ were nearly equiaxed, and their average size increased gradually with the increase of welding current. Simultaneously, the mechanical properties of the joints decreased with the increase of welding current under the set conditions of this experiment. The optimum mechanical properties of the joints were obtained at a welding current of 100 A. Their ultimate tensile strength (UTS), yield strength (YS), and elongation (EL) were 230 MPa, 103 MPa, and 19.2%, respectively, while the joint efficiency ($\sigma_b$ / $\sigma_b^{BM}$) was only 77.7%. The fracture locations of all the joints were found in the FZ. Excessive grain size was one of the significant factors contributing to the weakness of this zone. In addition, the semicontinuous second phase on the grain boundary induced high-stress concentrations, contributing to the fracture of the welded joint. The tensile properties of the joints can be improved by limiting heat input.



## Keywords

- Welding Current
- Welded Joints
- Fusion Zone
- Microstructure
- Mechanical Properties

*https://doi.org/10.29391/2025.104.002*


## Introduction

In the global efforts to achieve carbon neutrality, the development of magnesium alloy as the lightest structural metal has attracted more and more attention (Ref. 1). Magnesium alloys have a strong potential for development with high specific strength, excellent vibration-damping properties, and recyclability (Ref. 2). These advantages facilitate their application in automotive, aerospace, and electrocommunication (Ref. 1). Consequently, sophisticated magnesium alloy structural parts are bound to encounter challenges with joining technology. However, due to the poor weldability of magnesium alloy (Ref. 3), welding has become one of the bottleneck technical problems affecting the broader application of magnesium alloy.

Recently, many scholars have employed various welding techniques to study magnesium alloy joining. Some of these magnesium alloy welding techniques are also becoming more mature and typically include gas tungsten arc welding (GTAW), resistance spot welding (RSW), friction stir welding (FSW), laser beam welding, and electron beam welding (Ref. 3). GTAW is widely utilized in magnesium alloy joining because of its high flexibility and low cost (Ref. 4). Many efforts have been made to investigate the GTAW of magnesium alloys. Liu and Dong (Ref. 5) observed the microstructure and fracture of AZ31 magnesium alloy GTA-welded joints. It was shown that the grain size in the heat-affected zone (HAZ) of the welded joints filled with wire varied considerably compared to that of the welded joints not filled with wire. Moreover, the change in the HAZ's microstructure altered the fracture location and strength of the joints. The effect of heat input on the microhardness distribution of AZ61 magnesium alloy GTA-welded joints was studied by Xu et al. (Ref. 6). The welding heat input induced different microhardness distributions at the top and bottom of the welded joints. A combination of grain size and dispersion strengthening determined this. The microstructure of the GTA-welded joints for AZ91 mag-

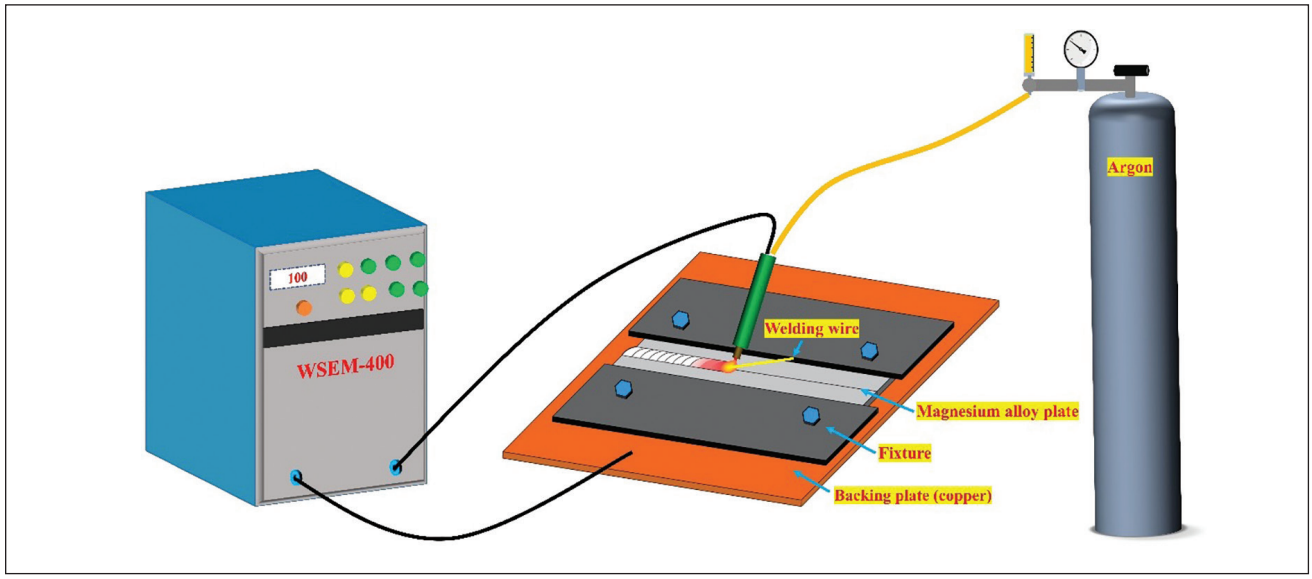


*Fig. 1 — Schematic diagram of the welding platform.*

nesium alloy was investigated by Braszczyńska-Malik et al. (Ref. 7). The width, depth, and dendrite arm size of the fusion zone (FZ) decreased with the increase in welding speed. In addition, Min and Shen et al. (Refs. 8, 9) explored the effects of heat input and preheat treatments on the microstructure and mechanical properties of tungsten inert gas arc-welded AZ61 magnesium alloy plates. Chen and Zhou et al. (Refs. 10, 11) also investigated the GTAW of AZ91D magnesium alloy. However, the existing GTAW investigations of magnesium alloys focus on AZ-series alloys, while few relevant works are on Mg-Zn series magnesium alloys.

As one of the two main alloying elements of magnesium alloy, the strengthening effect of Zn is quite conspicuous (Ref. 12). The Mg-Zn series magnesium alloys are an interesting path for developing high-strength and tough magnesium alloys. Specifically, the Mg-Zn-Y alloys have gathered a lot of attention. Y is one of the elements with a relatively large degree of solid solution in magnesium alloy (Ref. 13). The high solid solubility of Y makes the alloy form a supersaturated solid solution, acting as a strong solid solution and age-strengthening. The alloy is currently used in mechanical structural components and biomedical devices (Ref. 14). Previous studies have revealed that the phase constitution in Mg-Zn-Y alloys highly depends on the Zn/Y ratio (Ref. 15). Three ternary equilibrium phases exist in Mg-Zn-Y alloys, namely $Mg_3Zn_6Y$ (I-phase icosahedral quasi-crystal structure and quasi-periodic order), $Mg_3Zn_3Y_2$ (W-phase face-centered cubic structure) and $Mg_{12}ZnY$ (X-phase long period stacked ordered structure) (Ref. 16). The I-phase is characterized by high strength, high hardness, low coefficient of friction, and low interfacial energy (Ref. 16). The W-phase is usually distributed at the grain boundaries of magnesium alloys, and its addition in appropriate amounts can enhance the mechanical properties of the alloy (Ref. 17). The X-phase, with its unique crystalline structure, coherent interfaces with the Mg matrix, and the formation of kink bands, also significantly enhances the strength of the alloys (Ref. 16). The low Y content of Mg-Zn-Y alloys could reduce the cost of expensive rare earth elements. Therefore, Mg-Zn-Y alloys containing I-phase or W-phase have turned out to be a hot topic of discussion. Xu et al. (Ref. 17) investigated the microstructure and mechanical properties of the cast Mg-Zn-Y-Zr magnesium alloy with a Zn/Y ratio of about 0.97. The studies showed that the coarsened W-phase at the grain boundaries deteriorates the mechanical properties of the alloy. The effects of yttrium addition on the microstructure and mechanical properties of extruded Mg-Zn-Y-Zr magnesium alloys were investigated by Chen et al. (Ref. 18). The addition of Y led to the formation of W-phases distributed at grain boundaries and inside grains. Moreover, the addition of Y improved the yield strength (YS) of Mg-Zn-Y-Zr alloys, but the improvement of ultimate test strength (UTS) was not significant. Chen et al. (Ref. 19) employed a dual-frequency ultrasonic field to refine quasi-crystal-reinforced Mg-Zn-Y alloy. The results revealed that the dual-frequency ultrasonic field treatment could remarkably refine the Mg grains and I-phase. Thus, the corrosion resistance and mechanical properties of the material were improved. The microstructure and mechanical properties of as-cast Mg-6Zn-1.2Y alloy at room and elevated temperatures were studied by Jung et al. (Ref. 20). The coherent interface of the I-phase and α-Mg phase allowed the alloy to have superior tensile and creep properties.

With the development of Mg-Zn-Y alloy applications, welding this series of alloys will undoubtedly be a pressing

**Table 1 — Chemical Compositions of the ZW61 Alloy (wt-%)**

| Material | Elements | | | |
|---|---|---|---|---|
| | Zn | Y | Zr | Mg |
| ZW61 | 5.93 | 0.90 | 0.49 | Bal. |

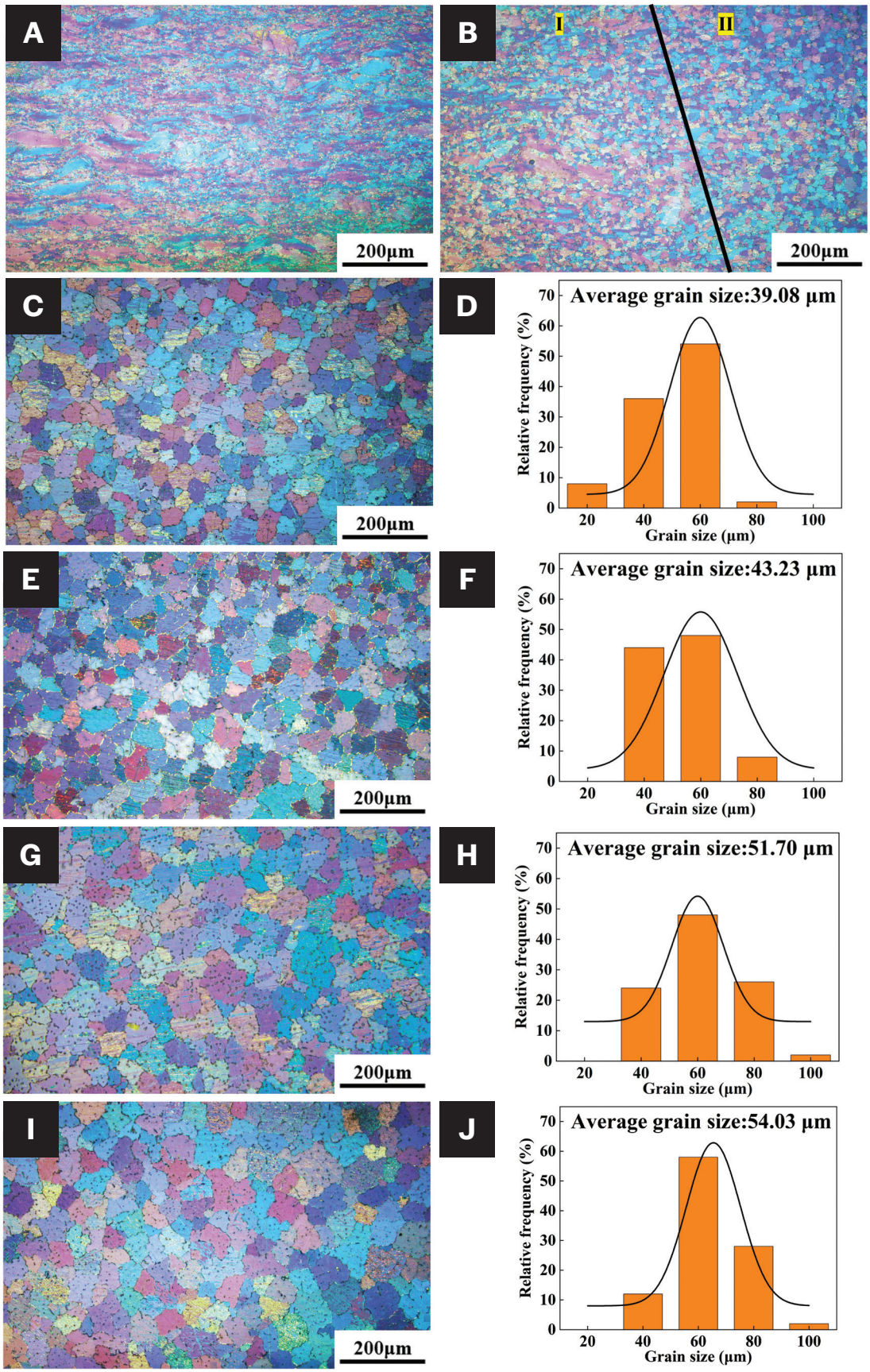


*Fig. 2 — Microstructure of the welded joints: A — BM, 100 A; B — HAZ, 100 A; C and D — FZ, 100 A; E and F — FZ, 110 A; G and H — FZ, 120 A; I and J — FZ, 130 A.*

**Table 2 — The Main Welding Parameters Used in the Test**

| Current (A) | Voltage (V) | Speed (mm/min) | Gas Flow (L/min) | Heat Input (J/mm) |
|---|---|---|---|---|
| 100 | 10 | 110 | 12 | 355 |
| 110 | 10 | 110 | 12 | 390 |
| 120 | 10 | 110 | 12 | 425 |
| 130 | 10 | 110 | 12 | 461 |

challenge. Currently, the welding of Mg-Zn-Y alloys is dominated by FSW (Ref. 21) with little research on arc welding. Consequently, GTAW was carried out for the ZW61 magnesium alloy in this paper. Welding current is one of the critical factors affecting the microstructure and properties of GTA-welded joints for magnesium alloys. Accordingly, the effect of welding current on the microstructure and mechanical properties of ZW61 magnesium alloy GTA-welded joints was discussed in detail. Meanwhile, the welded joints' microstructure evolution and softening mechanism were concretely analyzed.

## Experimental Method

### Welding Materials

The test base material (BM) was the as-extruded ZW61 magnesium alloy plate of 2 mm thickness. Welded specimens were prepared by a wire-cutting process of 200 mm × 40 mm × 2 mm. The composition of the welding wire was the same as that of the BM. The chemical composition of ZW61 magnesium alloy is shown in Table 1. Before the welding experiment, the surface of the magnesium alloy plate was sandpapered to remove the oxide film on the surface. Then, it was cleaned with acetone to remove the residual metal powder and oil on the surface.

### Welding Process

A WSME-400 pulsed AC/DC argon arc welder was used to conduct the welding. The current type and polarity were sinusoidal AC. The tungsten electrode and nozzle diameters were 2.3 and 8 mm, respectively. The joint type was the butt joint, and the joint was not beveled. The schematic diagram of the welding platform is shown in Fig. 1. A copper plate was placed on the back side of the magnesium alloy plate to expedite heat dissipation. Furthermore, the inert gas (argon) was supplied during welding to shield the weld area. The main welding parameters, such as welding current, welding speed, welding voltage, gas flow, and welding heat input (calculated from Equation 1 [Refs. 22–23]), are shown in Table 2.

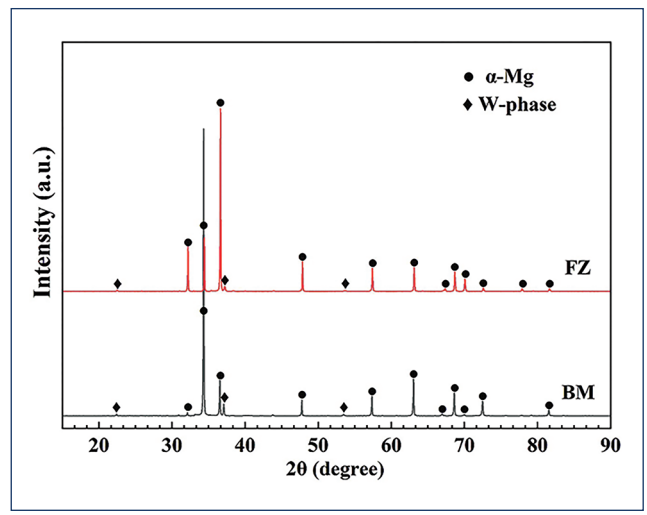


*Fig. 3 — XRD patterns of the BM and FZ.*

$$E=\eta UI/V \quad (1)$$

where η = 0.65 is the thermal efficiency coefficient (Refs. 22–23), $I$ is the welding current, $U$ is the welding voltage, and $V$ is the welding speed.

### Characterization

A specimen block of 20 mm × 5 mm was intercepted at the joint in the direction perpendicular to the weld as a metallographic specimen. After grinding and polishing, the metallographic specimen was etched with an etching solution (2 g picric acid + 10 ml glacial acetic acid + 10 ml distilled water + 75 ml ethyl alcohol). The optical microstructure of the welded joints was observed with an Olympus BX53-P polarizing microscope. The phase composition was identified by x-ray diffraction (XRD) with scanning angles of 15~90 deg and a scanning speed of 5 deg/min. Morphology and distribution of the phases and fracture morphology were performed by a field emission scanning electron microscope (SEM, Thermo Scientific Apreo 2) equipped with an ener-

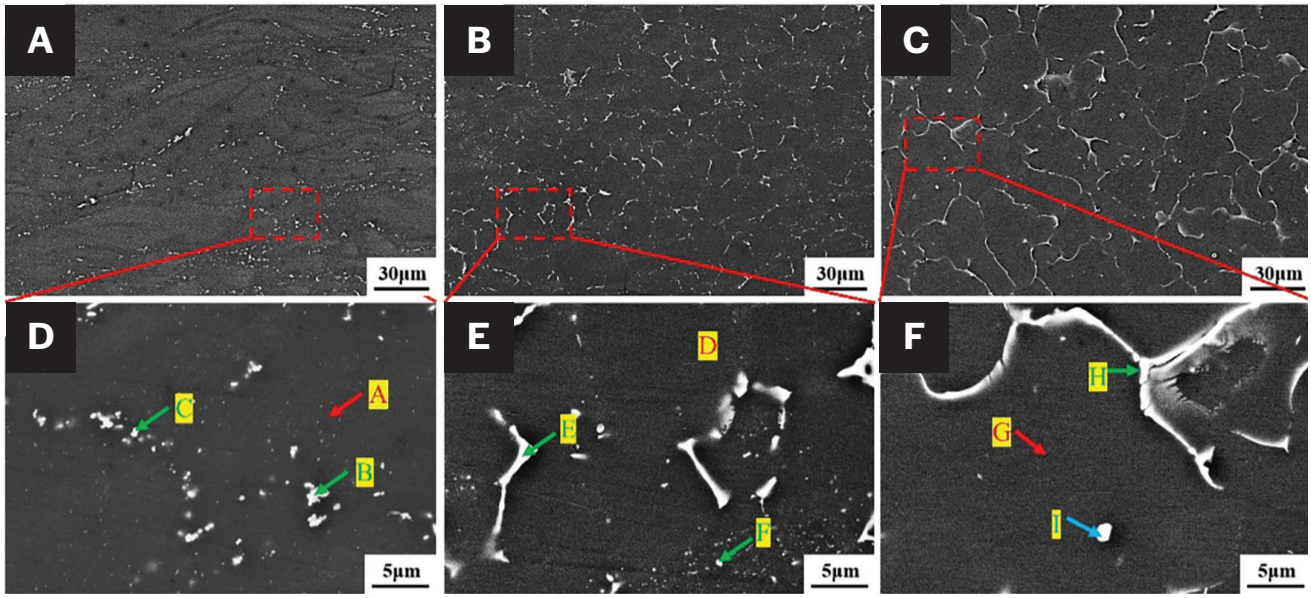


*Fig. 4 — SEM images of various zones of the welded joints with a welding current of 100 A: A and D — BM; B and E — HAZ; C and F — FZ.*

**Table 3 — Results of the EDS Analysis in Fig. 4. (at.-%)**

| Position | Mg | Zn | Y | Zr |
|---|---|---|---|---|
| A | 98.20 | 1.75 | 0.00 | 0.05 |
| B | 61.63 | 25.94 | 12.16 | 0.27 |
| C | 81.74 | 12.18 | 6.08 | 0.00 |
| D | 98.32 | 1.42 | 0.13 | 0.13 |
| E | 58.15 | 27.79 | 13.38 | 0.68 |
| F | 89.97 | 6.86 | 2.98 | 0.19 |
| G | 99.21 | 0.67 | 0.02 | 0.10 |
| H | 65.32 | 23.61 | 10.81 | 0.26 |
| I | 85.71 | 11.52 | 2.76 | 0.01 |

gy-dispersive spectroscope (EDS). The microhardness of each area of the welded joint was measured by a Vickers hardness tester (MH-5L) with a 200 gf load for 10 s. The tensile test was performed on an electronic universal material testing machine (AG-X100KN) with a 0.5 mm/min speed. To ensure the stability of the experimental results, the same mechanical experimental test was repeated three times.

## Results

### Microstructures

The microstructures of the GTA-welded joints for ZW61 alloys are shown in Fig. 2. The welded joints mainly included in the BM, HAZ, and FZ. As can be seen from Fig. 2A, most of the grains in the BM were elongated by extrusion. A few fine equiaxed grains were also involved. The opposite was confirmed in the HAZ, where the microstructure was almost entirely uniform and contained fine equiaxed grains, as

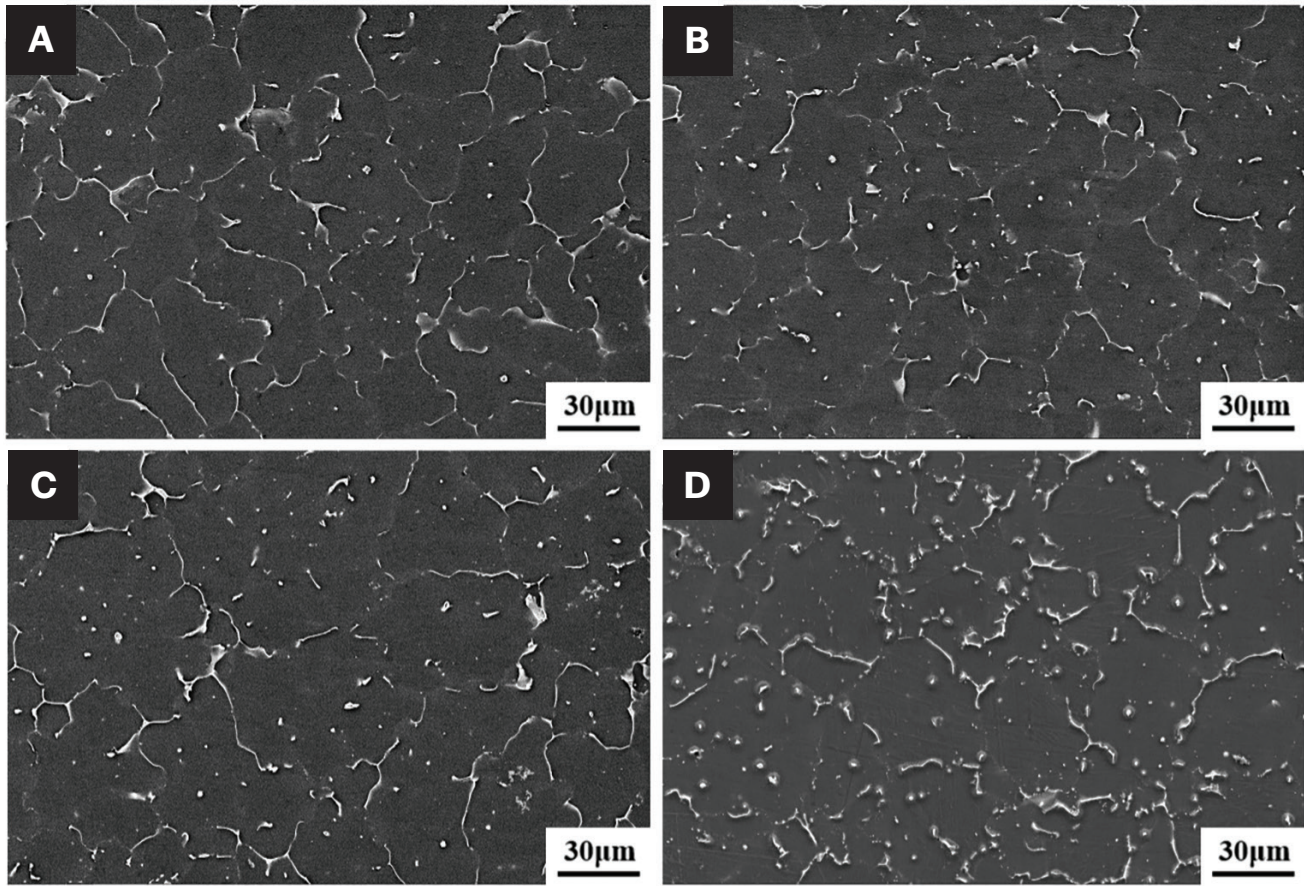


*Fig. 5 — SEM images of the FZ with different welding currents: A — 100 A; B — 110 A; C — 120 A; D — 130 A.*

presented in Fig. 2B. Only a few deformed grains could be observed. Figures. 2C–J demonstrate the microstructure of the FZ with different welding currents. All grains in the FZ were coarser and equiaxed, and the grain size increased with increasing current. The average grain size of the FZ was smallest at 39.08 μm when the welding current was 100 A. The average grain size of the FZ increased by 38% as the welding current increased to 130 A. As indicated by Equation 1, the increase in welding current inevitably caused a rise in welding heat input. At such a high heat input, the grain of the FZ was larger.

Figure 3 exhibits the XRD patterns of the FZ and BM. From the XRD patterns, no change in the type of the second phase of the FZ following welding was observed compared to that of the BM. The microstructure of the FZ was composed of α-Mg and W-phase ($Mg_3Zn_3Y_2$). The diffraction peak at 34.4 deg of the XRD pattern of the BM was significantly higher than other diffraction peaks. This was due to the forming of a stronger fiber texture in the ZW61 alloy during extrusion deformation.

The SEM images of various zones of the welded joints with a welding current of 100 A are presented in Fig. 4. Table 3 demonstrates the results of the corresponding EDS analysis. As shown in Fig. 4A, the second phase of the BM was distributed along the boundaries of the deformed grains in a granular shape. The EDS analysis results indicated that this second phase was a Mg-Zn-Y phase and the Zn/Y was about 1.5. Combined with the XRD results, this second phase was a W-phase. The shape and distribution of the second phase in the HAZ were entirely different from that of the second phase in the BM, as depicted in Fig. 4B. During the welding process, the temperature of the HAZ was much higher than the solid solution temperature of the W-phase under the action of the residual heat of welding. The W-phase was dissolved and reprecipitated during the welding process. The W-phase in the HAZ was mainly distributed in a semi-continuous network at the grain boundaries, as shown in Fig. 4E. Also, a portion of the second phase was distributed in the grain in the form of dots. Figures 4C and F display the shape and distribution of the second phase in the FZ. Like the HAZ, most of the second phases in this zone were distributed at the grain boundaries. However, this type of second phase was much more abundant and considerably coarser. Meanwhile, the EDS results showed that this phase was a W-phase, consistent with the XRD results. Moreover, a granular second phase existed within the grains. The EDS results indicated that this phase had a Zn/Y of about 4, from which it was inferred that this phase was an I-phase. As given in Fig. 4C, the I-phase was present in low amounts in the FZ, leading to no diffraction peaks of this phase being found in the XRD pattern.

Figure 5 displays the SEM images of the FZ with different welding currents. The change in welding current did not induce the shape and distribution of the second phase

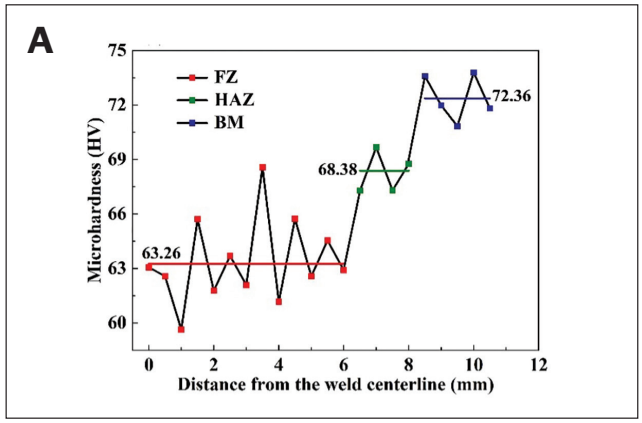


*Fig. 6 — A — Microhardness distribution of the welded joints from FZ to BM with welding current of 100A; B — statistical charts of microhardness in the FZ with different welding currents.*

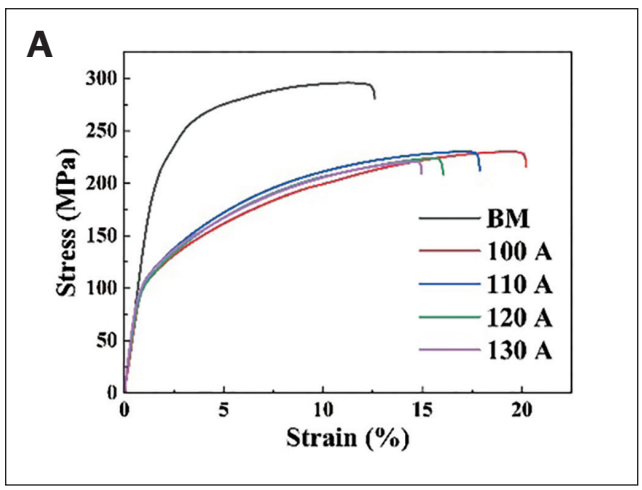


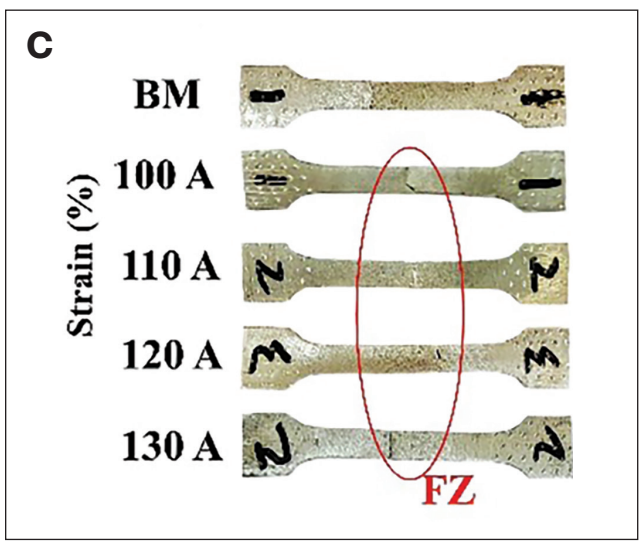


*Fig. 7 — A — Engineering stress-strain curves; B — the effect of welding current on tensile properties of the welded joints; C — fracture locations of the BM and welded joints.*

in the FZ. However, the increase in welding current elicited a less-pronounced increase in the second phase size. The amount of the second phase in the FZ increased gradually with the welding current, which was 2.52, 2.74, 3.20, and 3.93%, respectively. From the previous section, an increase in welding current increased welding heat input, further decelerating the cooling rate. At lower cooling rates, solute atoms had ample time to diffuse, ultimately leading to an increase in the volume fraction of the second phase at grain boundaries.

## Mechanical Properties

As displayed in Fig. 6A, the microhardness within each zone of the welded joint floated around a particular value without substantial change at a welding current of 100 A. However, the microhardness of different zones varied significantly; the microhardness of the BM had a maximum value of 72.36 HV, while the microhardness of the FZ had a minimum value of 62.36 HV. Larger grain size and lower dislocation density induced a marked decrease in the microhardness of the FZ. Fig. 6B presents the statistical charts of microhardness in the FZ with different welding currents. The FZ's microhardness decreased with an increase in welding currents, but the decrease was slight. The microhardness

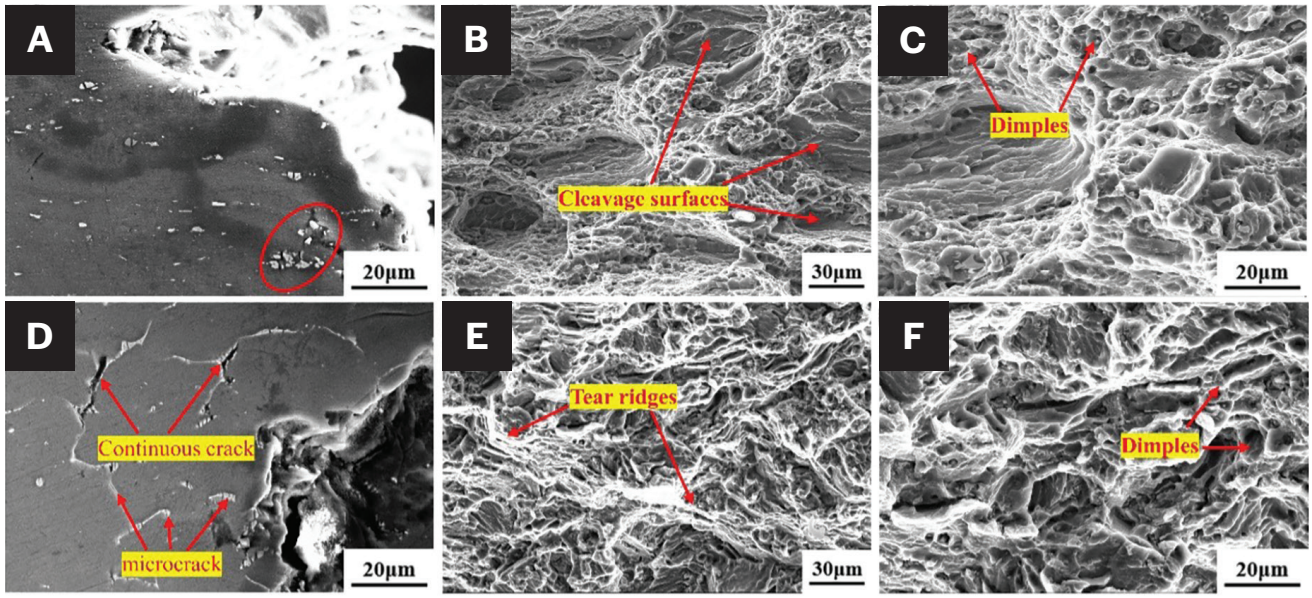


*Fig. 8 — Morphologies and longitudinal section of the fracture: A–C — BM; D–F — FZ.*

**Table 4 — Mechanical Properties of the BM and Welded Joints**

| | $\sigma_b$ (MPa) | $\sigma_s$ (MPa) | δ (%) | Joint Efficiency ($\sigma_b/\sigma_b^{BM}$) (%) |
|---|---|---|---|---|
| BM | 296 ± 4 | 195 ± 2 | 11.1 ± 0.2 | / |
| 100 A | 230 ± 1 | 103 ± 1 | 19.2 ± 0.2 | 77.7 |
| 110 A | 230 ± 1 | 102 ± 1 | 17.0 ± 0.2 | 77.7 |
| 120 A | 224 ± 2 | 98 ± 2 | 15.1 ± 0.1 | 75.7 |
| 130 A | 220 ± 1 | 97 ± 1 | 14.2 ± 0.1 | 74.3 |

of the FZ was minimized when the welding current was 130 A. The microhardness of the FZ was only degraded by 8% compared to that of the FZ with a welding current of 100 A.

Figures 7A and B demonstrate the tensile properties of the BM and welded joints. The corresponding data are shown in Table 4. The UTS, YS, and EL of ZW61 extruded magnesium alloy were 296 MPa,195 MPa, and 11.1%, respectively. In comparison, the UTS and YS of all welded joints were much weaker, but the EL improved considerably. As indicated in Fig. 7A, the UTS and YS of the welded joints did not fluctuate much with the increase in welding current. As displayed in Fig. 7B, the EL decreased gradually with the increase in the welding current. From Table 4, it can be summarized that the mechanical properties of the welded joints were optimal under the use conditions in this study (where the welding current was 100 A). The EL was significantly improved to 19.2% compared to the BM. However, the UTS and YS decreased by 22.3 and 47.2%, respectively. The joint efficiency was only 77.7%, which did not meet the service standard (90%) of welded joints. In addition, it can be seen from Table 4 that the poorest welded joint properties occurred at a welding current of 130 A. In this case, the UTS and YS of the welded joints decreased slightly compared to those of the optimized welded joints, but the EL decreased tremendously (26%). Figure 7C exhibits the fractured locations of the BM and welded joints. The weak location of all welded joints occurred in the FZ. Previous studies showed a weakness in a different location from the magnesium alloy GTA-welded joints (Refs. 24, 25) for reasons that will be detailed below.

Figure 8 shows the morphologies and longitudinal section of the fracture of the BM and welded joint. As indicated in Fig. 8A, cracks and micropores were formed at the second phase aggregation near the fracture. It was inferred that stress concentration was generated here during the tensile process. The presence of cleavage surfaces and dimples can be observed in Figs. 8B and C. The fracture of the BM exhibited a combination of brittleness and ductility, as evidenced by these features. However, the small amount and tiny size of the dimples on the fracture surface indicated that

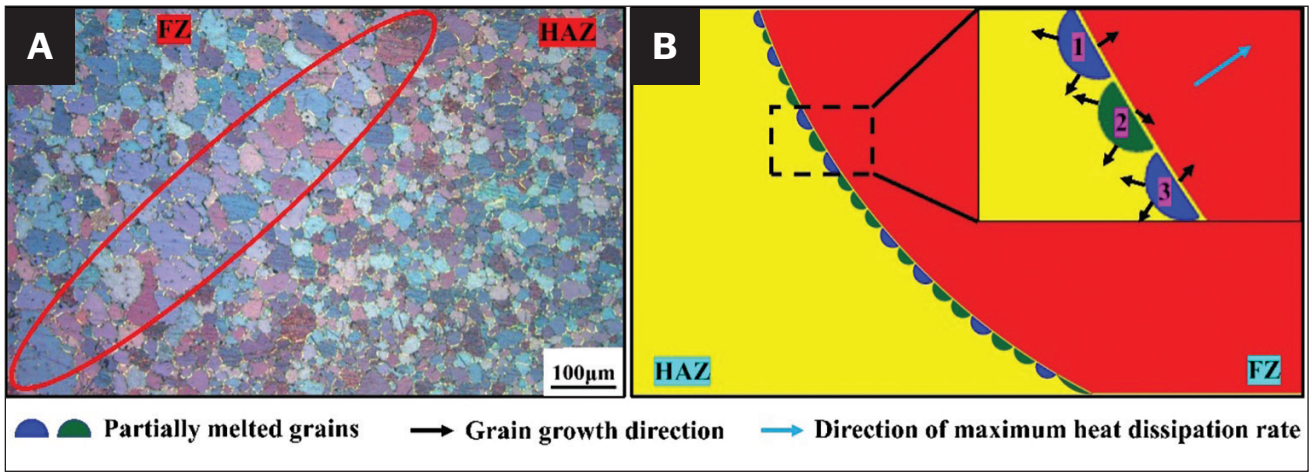


*Fig. 9 — A — Microstructure at the junction of the FZ and HAZ; B — schematic of grain growth at the junction of the FZ and HAZ.*

the fracture mode was dominated by brittle fracture and supplemented by ductile fracture. As illustrated in Fig. 8D, microcracks and continuous cracks nearly perpendicular to the tensile direction were generated at the location of the second phase at the grain boundary. The second phase was still preferred for stress concentration, which was consistent with the analysis of the BM. Meanwhile, the grains near the fracture were coarse equiaxed grains. This microstructure appeared only in the FZ of the welded joint, further proving the analysis in Fig. 7C. As shown in Figs. 7E and F, the fracture surfaces of the welded joints were characterized by cleavage surfaces, tear ridges, and dimples. However, the size of the cleavage surface was smaller, and the dimple's size was larger than that of the BM. These features supported the fact that the welded joints had superior plasticity to the BM, as shown in Fig. 7.

## Discussion

### Microstructure Evolution of the Welded Joint

As depicted in Fig. 2A, the microstructure of the BM mainly consisted of deformed grains, while there were few recrystallized grains. During the welding process, static recrystallization and potential grain growth of the deformed grains in the HAZ occurred under the effect of welding heat. The energy provided by welding heat only supported recrystallization nucleation and initial growth. Therefore, the HAZ did not exhibit excessive grain size, as shown in Fig. 2B. Furthermore, as the distance from the center of the weld increased, the heat received at each location of the HAZ was different, which resulted in a variable degree of recrystallization at each location. Some zones were wholly recrystallized (Fig. 2B–II), while some zones still had the presence of deformed grains (Fig. 2B–I). Also, the size of the recrystallized grains in all regions of the HAZ was much less than the size of the grains in the FZ.

Most heat absorbed by the welded joint was supplied to the FZ, where solidification, epitaxial regrowth, and competitive growth occurred. The grain size of the FZ was mainly controlled by the temperature gradient (G) and solidification growth rate (R) at the solid/liquid interface front during solidification in the molten pool. G·R characterizes the cooling rate of the solidification process and affects the microstructure scale. Under the condition of constant welding speed, the G·R value tended to decrease with the increase of welding heat input, thus leading to an increase in the grain size of the FZ. From Figs. 2C–J, most of the grain size in the FZ exceeded 40 μm. This was an essential factor contributing to the FZ being the weakest position of the welded joint. In addition, as shown in Fig. 9A, there was a region with the largest grain size at the junction of the HAZ and FZ. This phenomenon has also appeared in previous studies (Ref. 26) and presupposes that the welding wire is made of the same material as the BM. As displayed in Fig. 9B, some grains were only partially melted in this region. Some partially melted grains grew in the direction of maximum heat dissipation rate, such as grains 1 and 3, and these grains grew preferentially. Some grains grew in other directions, such as grain 2, which were restricted or engulfed. Meanwhile, the temperature in this region exceeded the liquation temperature of the second phase. Without the limitation of the second phase, the grains also grew further in other directions. However, the growth rate along these directions was slighter than that along the direction with the maximum heat dissipation rate.

Compared with AZ series magnesium alloys, ZK series magnesium alloys have a wider crystallization temperature interval, which makes it easy to form thermal cracks during welding (Ref. 27). After adding the Y element to the ZK alloy, the Y element can change the dissolution degree of Zn, thus improving the weldability of the alloy (Ref. 17). Simultaneously, the Y element affects grain refinement in the ZK alloy (Ref. 28). However, in this experiment, due to the high content of alloying elements, the W-phase mainly existed in the form of a network, significantly weakening this effect. Moreover, under the conditions of different welding currents set in this experiment, the change of W-phase content was inconspic-

uous, as shown in Fig. 5. Therefore, the effect of W-phase on the microstructure of the welded joint was minimal. Welding heat input was the main factor causing changes in the grain size of the FZ.

## Weakening Mechanism of the Welded Joint

Fine-grain strengthening is one of the most essential strengthening mechanisms for magnesium alloys. Grain coarsening significantly deteriorates the strength of magnesium alloys. In this experiment, the size of the grains in the HAZ was much less than that in the FZ. Therefore, unlike most of the previous studies (Refs. 24, 25), the weak location of the welded joints in this experiment was the FZ. As shown in Figs. 2C–F, the average grain size of the FZ rose with the increase of welding current. However, the strength of the welded joint did not decrease significantly, which is well explained by the Hall-Petch formula (Ref. 29). Calculated from Equation 2, the differences in strength with increasing welding current are 2.2, 5.8, and 6.7 MPa, consistent with the experimental results. Additionally, the size of the grains significantly contributes to the plasticity of the welded joint. Finer grains result in more grains taking on plastic deformation in a given volume. Uniform deformation yields low-stress concentrations. Also, fine grains have zigzag grain boundaries that are not conducive to crack propagation. Therefore, as the welding current increases, the EL of the welded joints decreases.

$$\sigma_y = \sigma_0 + k d^x \quad (2)$$

where $\sigma_y$ is the yield stress, $\sigma_0$ is the stress for dislocation motion in grain interior, and k is the Hall-Petch slope (0.28 MPa·m$^{1/2}$) (Ref. 30), $d$ is the grain diameter, and $x$ is the exponent, which is close to $-1/2$ for random crystallographic textures and close to $-1$ for many solidification structures due to texturing.

As depicted in Fig. 5, the second phase with a semicontinuous network was distributed at the grain boundaries in the FZ. The location of the second phase on the grain boundaries is often a point of stress concentration (Refs. 30, 31). Under high tensile stresses, microcracks can develop at such positions. Microcracks link up to form continuous cracks, inducing fracture in welded joints, as indicated in Fig. 8D. Therefore, the second phase at the grain boundary is another vital factor in the deterioration of the mechanical properties of the welded joints.

# Conclusions

In this paper, the ZW61 magnesium alloy extruded plate was successfully welded using GTAW. The influence rule of the welding current on the microstructure and mechanical properties of the welded joints was analyzed. The specific conclusions were as follows:

1. The grains were uniform and fine in the HAZ of the welded joints. On the other hand, most of the grains in the FZ exceeded 40 μm in size. In addition, the welding heat input increased with the increase in welding current, which led to an increase in grain size.
2. In the FZ of the welded joints, the microstructure consisted of α-Mg, I-$Mg_3Zn_6Y$ and W-$Mg_3Zn_3Y_2$ phases. The I-phase was distributed inside the grains in a granular form, and the W-phase was distributed at the grain boundaries in a semicontinuous network.
3. As the welding current increased, the strength of the welded joints changed insignificantly, but the EL decreased gradually. Under the set conditions of this experiment, the welded joint with optimum mechanical properties was formed at a welding current of 100 A, and its UTS, YS, and EL were 230 MPa, 103 MPa, and 19.2%, respectively. In contrast, the joint efficiency was only 77.7%.
4. The FZ was the weakest position of a welded joint. Excessive grain size was one of the significant factors contributing to the weakness of this zone. Furthermore, the semicontinuous second phase at the grain boundary induced high-stress concentrations, leading to the fracture of the welded joint. The tensile properties of the joints can be improved by limiting heat input.

### *Acknowledgments*

This research was financially supported by the National Natural Science Foundation of China (Grant No. 51974082, 52274377, 52304391) and the Natural Science Foundation of Liaoning Province, China (Grant No. 2023-MSBA-133).

### *References*

1. Zeng, Z., Stanford, N., and Davies, C. H. J., et al. 2019. Magnesium extrusion alloys: a review of developments and prospects. *International Materials Reviews* 64: 27-s to 62-s. DOI: 10.1080/09506608.2017.1421439

2. Huang, Z., Qi, C., and Zou, J., et al. 2023. Edge crack damage analysis of AZ31 magnesium alloy hot-rolled plate improved by vertical roll pre-rolling. *Journal of Magnesium and Alloys* 11: 2151-s to 2164-s. DOI: 10.1016/j.jma.2021.08.038

3. Czerwinski, F. 2011. Welding and joining of magnesium alloys. *Magnesium Alloys – Design, Processing and Properties*. DOI: 10.5772/13947

4. Liu, L. M. 2010. Welding and joining of magnesium alloys. *Woodhead Publishing Series in Welding and Other Joining Technologies*. DOI: 10.1533/9780857090423.1.38

5. Liu, L. M., and Dong, C. F. 2006. Gas tungsten-arc filler welding of AZ31 magnesium alloy. *Materials Letters* 60: 2194-s to 2197-s. DOI: 10.1016/j.matlet.2005.12.120

6. Xu, N., Shen, J., and Xie, W. D., et al. 2010. Abnormal distribution of microhardness in tungsten inert gas arc butt-welded AZ61 magnesium alloy plates. *Materials Characterization* 61: 713-s to 719-s. DOI: 10.1016/j.matchar.2010.04.003

7. Braszczyńska-Malik, K.N., and Mróz, M. 2011. Gas-tungsten arc welding of AZ91 magnesium alloy. *Journal of Alloys and Compounds* 509: 9951-s to 9958-s. DOI: 10.1016/j.jallcom.2011.07.105

8. Min, D., Shen, J., Lai, S., and Chen, J. 2009. Effect of heat input on the microstructure and mechanical properties of tungsten inert gas

arc butt-welded AZ61 magnesium alloy plates. *Materials Characterization* 60: 1583-s to 1590-s. DOI: 10.1016/j.matchar.2009.09.010

9. Shen, J., and Xu, N. 2012. Effect of preheat on TIG welding of AZ61 magnesium alloy. *International Journal of Minerals, Metallurgy, and Materials* 19: 360-s to 363-s. DOI: 10.1007/s12613-012-0564-8

10. Zhou, W., Long, T. Z., and Mark, C. K. 2007. Hot cracking in tungsten inert gas welding of magnesium alloy AZ91D. *Materials Science and Technology* 23: 1294-s to 1299-s. DOI: 10.1179/174328407X213026

11. Chen, Y., Fan, C., Lin, S., and Yang, C. 2023. Effect of tungsten inert gas welding parameters on hot crack sensitivity of cast magnesium alloy. *Journal of Materials Engineering and Performance* 32: 1382-s to 1389-s. DOI: 10.1007/s11665-022-07192-7

12. Zhang, E., Yin, D., and Xu, L., et al. 2009. Microstructure, mechanical and corrosion properties and biocompatibility of Mg–Zn–Mn alloys for biomedical application. *Materials Science and Engineering*: C 29: 987-s to 993-s. DOI: 10.1016/j.msec.2008.08.024

13. Yin, S., Zhang, Z., and Liu, X., et al. 2019. Effects of Y content on the microstructures and mechanical properties of Mg-5Zn-xY-0.6Zr Alloys. *Journal of Wuhan University Technology-Materials Science* 34: 138-s to 144-s. DOI: 10.1007/s11595-019-2027-9

14. Sun, M., Cheng, G., and Li, X., et al. 2024. Research status and prospect of Mg-Zn-Y magnesium alloys. *Nonferrous Metal Materials and Engineering* 45: 66-s to 77-s.

15. Liu B., Yang J., Wang Z., and Fang D. 2020. Effect of Y/Zn ratio on microstructure and properties of as-extruded Mg-Y-Zn alloys. *Materials Research Express* 7: 036530. DOI: 10.1088/2053-1591/ab8094

16. Tahreen, N., Zhang, D. F., and Pan, F. S., et al. 2018. Strengthening mechanisms in magnesium alloys containing ternary I, W and LPSO phases. *Journal of Materials Science & Technology* 34: 1110-s to 1118-s. DOI: 10.1016/j.jmst.2017.12.005

17. Xu D. K., Tang, W. N., and Liu, L., et al. 2008. Effect of W-phase on the mechanical properties of as-cast Mg–Zn–Y–Zr alloys. *Journal of Alloys and Compounds* 461: 248-s to 252-s. DOI: 10.1016/j.jallcom.2007.07.096

18. Chen, M. B., Pan, F. S., and Wang, J. F., et al. 2010. Effects of yttrium addition on microstructure and mechanical properties of extruded Mg-Zn-Y-Zr magnesium alloys. *Materials Science Forum* 650: 279-s to 284-s. DOI: 10.4028/www.scientific.net/MSF.650.279

19. Chen, X., Ning, S., and Wang, A., et al. 2020. Microstructure, mechanical properties and corrosion behavior of quasicrystal-reinforced Mg-Zn-Y alloy subjected to dual-frequency ultrasonic field. *Corrosion Science* 163: 108289. DOI: 10.1016/j.corsci.2019.108289

20. Jung, Y. G., Yang, W., and Hyun, J. I., et al. 2021. Effects of I- and W-Phases under identical conditions on microstructure and mechanical properties of as-cast Mg–Zn–Y alloys at room and elevated temperatures. *Metals and Materials International* 27: 5154-s to 5164-s. DOI: 10.1007/s12540-020-00848-w

21. Wang, Y., Huang, Y., and Meng, X., et al. 2017. Microstructural evolution and mechanical properties of Mg-Zn-Y-Zr alloy during friction stir processing. *Journal of Alloys and Compounds* 696: 875-s to 883-s. DOI: 10.1016/j.jallcom.2016.12.068

22. Xu, N., Shen, J., and Xie, W. D., et al. 2010. Abnormal distribution of microhardness in tungsten inert gas arc butt-welded AZ61 magnesium alloy plates. *Materials Characterization* 61: 713-s to 719-s. DOI: 10.1016/j.jmatchar.2010.04.003

23. Li, Y. J. 2005. *Performance and quality control of the welding*. Beijing: Chemical Industry Press.

24. Xu, N., Bao, Y. 2016. Enhanced mechanical properties of tungsten inert gas welded AZ31 magnesium alloy joint using two-pass friction stir processing with rapid cooling. *Materials Science and Engineering*: A 655 :292-s to 299-s. DOI: 10.1016/j.msea.2016.01.009

25. Liu, X., Gu, S., and Wu, R., et al. 2011. Microstructure and mechanical properties of Mg-Li alloy after TIG welding. *Transactions of Nonferrous Metals Society of China* 21: 477-s to 481-s. DOI: 10.1016/S1003-6326(11)60739-5

26. Zhou, W., Le, Q., and Ren, L., et al. 2023. Effect of welding current and Laves phase on the microstructures and mechanical properties of GTAW joints for ZC63 magnesium alloy. *Materials Science and Engineering*: A 872: 144954. DOI: 10.1016/j.msea.2023.144954

27. Chen, Z. H. 2005. *Wrought magnesium alloys*. Beijing: Chemical Industry Press.

28. Ma, C., Liu, M., and Wu, G., et al. 2003. Tensile properties of extruded ZK60-RE alloys. *Materials Science and Engineering*: A 349: 207-s to 212-s. DOI: 10.1016/S0921-5093(02)00740-2

29. Xu, J., Guan, B., Xin, Y., et al. 2022. A weak texture dependence of Hall–Petch relation in a rare-earth containing magnesium alloy. *Journal of Materials Science & Technology* 99: 251-s to 259-s. DOI: 10.1016/j.jmst.2021.04.076

30. Lotfpour, M., Emamy, M., Dehghanian, C., and Tavighi, K. 2017. Influence of Cu addition on the structure, mechanical and corrosion properties of cast Mg-2%Zn alloy. *Journal of Material Engineering and Performance* 26: 2136-s to 2150-s. DOI: 10.1007/s11665-017-2672-0

31. Liu, Y., Deng, C., Gong, B., and Bai, Y. 2019. Effects of heterogeneity and coarse secondary phases on mechanical properties of 7050-T7451 aluminum alloy friction stir welding joint. *Materials Science and Engineering: A* 764: 138223. DOI: 10.1016/j.msea.2019.138223

**WEIYANG ZHOU, QICHI LE** (qichil@mail.neu.edu.cn), **YE SHI**, and **TONG WANG** are with Key Lab of Electromagnetic Processing of Materials, Ministry of Education, Northeastern University, Shenyang, China. **QIYU LIAO** is with School of Materials Science and Engineering, Northeastern University, Shenyang, China, as well as with Key Laboratory of Lightweight Structural Materials, Liaoning Province, Northeastern University, Shenyang, China. **WENXIN HU** is with Baotou Research Institute of Rare Earths, Baotou, China.